Grain-Boundary Resistance in Copper Interconnects: From an Atomistic Model to a Neural Network

Daniel Valencia* and Evan Wilson
School of Electrical and Computer Engineering, Network for Computational Nanotechnology, Purdue University, West Lafayette, Indiana 47907, USA

Zhengping Jiang
Samsung Semiconductor Inc., San Jose, California 95134, USA

Gustavo A. Valencia-Zapata and Kuang-Chung Wang
School of Electrical and Computer Engineering, Network for Computational Nanotechnology, Purdue University, West Lafayette, Indiana 47906, USA

Gerhard Klimeck
School of Electrical and Computer Engineering, Network for Computational Nanotechnology, Purdue University, West Lafayette, Indiana 47906, USA and Birck Nanotechnology Center, Network for Computational Technology, Purdue University, West Lafayette, Indiana 47907, USA

Michael Povolotskyi
Birck Nanotechnology Center, Network for Computational Technology, Purdue University, West Lafayette, Indiana 47907, USA

(Received 20 January 2017; revised manuscript received 28 November 2017; published 4 April 2018)

Orientation effects on the specific resistance of copper grain boundaries are studied systematically with two different atomistic tight-binding methods. A methodology is developed to model the specific resistance of grain boundaries in the ballistic limit using the embedded atom model, tight- binding methods, and nonequilibrium Green's functions. The methodology is validated against first-principles calculations for thin films with a single coincident grain boundary, with 6.4% deviation in the specific resistance. A statistical ensemble of 600 large, random structures with grains is studied. For structures with three grains, it is found that the distribution of specific resistances is close to normal. Finally, a compact model for grain-boundary-specific resistance is constructed based on a neural network.

DOI: 10.1103/PhysRevApplied.9.044005

I. INTRODUCTION

Because of the aggressive downscaling of logic devices, interconnects have reached the nanoscale, making quantum effects important. According to the road map provided by ITRS, interconnects are expected to reach sizes of 10 to 30 nm in the next decade [1]. Previous work by Graham *et al.* [2] demonstrates that surface scattering and grain-boundary (GB) scattering play major roles in the resistance of structures smaller than 50 nm. Earlier works based on semiempirical parameters have described polycrystalline films and surface scattering [3,4] for macroscopic systems, but the fact that those models require fitting parameters for each experimental setup limits the scope of their applications. The ultrascaled interconnects suggested by the road map require better descriptions of orientation and confinement effects to correctly model scattering in wires. Recently, first-principles calculations have been used to describe the resistance of a single grain boundary by making use of the nonequilibrium Green's function with density-functional-theory (DFT NEGF) formalism [5]. The results demonstrate a strong correlation between resistance and the geometry of the grain boundary and show agreement with both experimental [6] and other theoretical work [7–9]. However, the studied structures are limited to relatively small sizes containing single grain boundaries and less than a few hundred atoms because of the computational burden required to perform DFT NEGF calculations.

The purpose of this manuscript is to introduce an atomistic model that describes the specific resistance due to grain-boundary effects for realistic copper interconnects as projected by the ITRS road map [1] without depending on any phenomenological parameter. Even though the atomistic model is much faster than an *ab initio* method,

*valencid@purdue.edu

parametric models have the advantage of easily providing a quantitative value of specific resistance. Therefore, a compact model which reduces the computation time is generated by making use of a neural network that is based on a large statistical sample. The rest of the manuscript is organized as follows. Section II presents the main characteristics of the atomistic models and benchmarks tight-binding parameters against first-principles calculations for a copper fcc structure. Section III constructs single grain boundaries based on a coincident site lattice (CSL) and validates their electronic properties against an *ab initio* method. Section IV describes grain-boundary effects on copper interconnects using a system of three grains of 10 nm length simulated with an atomistic method which is benchmarked in the previous sections and quantifies the effect of misorientation. Section V proposes a compact model based on three different algorithms and finds that a neural network approach best matches the results obtained from the atomistic methods, allowing the results to be generalized to any grain-boundary system configuration with a total length of 30 nm. Section VI presents a summary of this work.

II. DESCRIPTION OF TIGHT-BINDING MODELS

The two tight-binding methods used in this study are an environmental orthogonal tight-binding (TB) model [10] and a nonorthogonal tight-binding method based on the extended Hückel (EH) model [11]. The TB model has an orthogonal basis with an interaction radius up to the second nearest neighbor (2NN 0.4 nm). However, it requires a large number of parameters to include strain effects (48 parameters for copper). In comparison, the EH model has a nonorthogonal basis with a larger interaction radius up the third nearest neighbor (3NN 1.0 nm). It requires a smaller number of parameters than the TB method (11 parameters for copper).

The existing parameters for the TB model [10] fail when used in highly distorted atomic systems such as GBs. Because of the exponential dependence of the interatomic coupling on the bond length, the interatomic matrix elements corresponding to bond lengths with a 5% or greater distortion generate unphysical results. The problem is solved by obtaining a parametrization with additional constraints on the interatomic coupling. This parameter set is summarized in Table II in the Appendix. The parameters for the EH model are taken from the literature [12]. Both EH parameters and the new TB parameters show a good match for the Cu unit cell when compared against an *ab initio* method as shown in Fig. 1. The *ab initio* result used as a reference is obtained by the density-functional method with a Perdew-Burke-Ernzerhof version of the generalized-gradient approximation (GGA PBE) exchange-correlation functional [13]. An energy cutoff of 150 Ry is used, and the Brillouin zone is sampled with a $10 \times 10 \times 10$ mesh. A fcc copper lattice with a lattice constant of 0.361 nm, as reported experimentally [14], is considered.

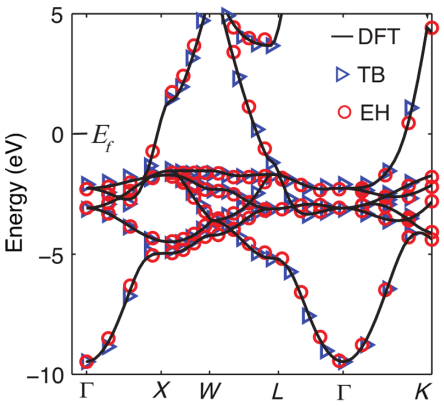

FIG. 1. Band structure for the copper unit cell obtained by the TB, EH, and DFT methods. E_f indicates the Fermi energy.

III. SINGLE-GRAIN-BOUNDARY CALCULATIONS

To validate the tight-binding models, the effects of GB scattering are studied for a single coincident site lattice (CSL) and random single (RS)-grain boundaries. The CSL GB configurations are obtained by a rotation of one of the grains until its lattice vector becomes coincident with the vector of the unrotated lattice [15], as shown in Fig. 2.

Additionally, our semiempirical methods are validated against highly distorted atomic systems as shown in Fig. 3. A fairly small number of atoms (<400) are required to construct these systems, which allows the tight-binding models to be benchmarked against a first-principles calculation as implemented in the ATK package [13]. The CSLs are labeled by ΣN, where N corresponds to the ratio of the CSL unit-cell size to the standard unit-cell size. In this work, the CSL GBs are generated with GBstudio [16], and the RS grain boundaries are generated by Voronoi diagrams [17]. Those structures are then relaxed using an *ab initio* method. The relaxation is carried out with a GGA PBE exchange-correlation functional. A double-ζ polarized basis set is used for copper atoms with an energy cutoff of 150 Ry and the Brillouin zone sampled with a $4 \times 4 \times 1$ mesh, until all atomic forces on each ion are less than 10^{-5} eV/Å. Once the ionic relaxation is completed, the transmission spectra for

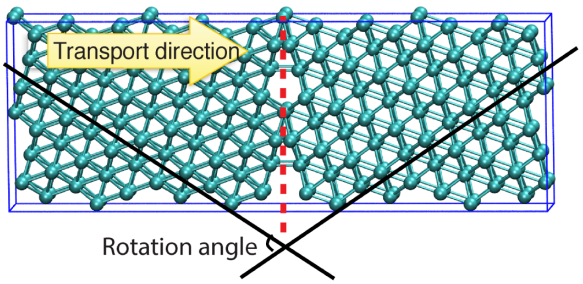

FIG. 2. Coincident site lattice GBs are obtained by generating a superposition of two periodic lattices. One of the lattices is rotated with respect to the other, generating coincident points between the lattices for each rotation angle.

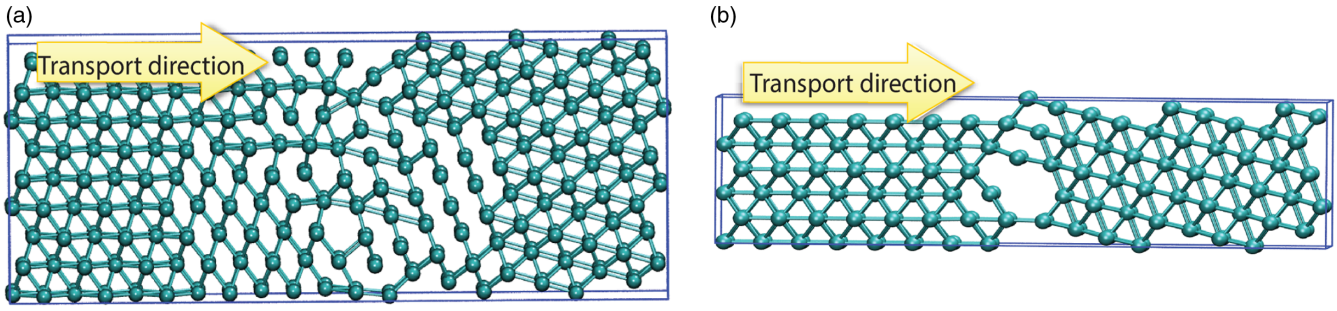

FIG. 3. Schematic representation of random single-grain boundaries. Structures (a) and (b) are obtained for copper atoms growing in the direction [111] with rotation angles in the directions $[\bar{1}\,\bar{1}\,2]$ and $[1\bar{1}0]$ by a a rotation equal to 78.4° and 70.5°, respectively.

the CSL and RS structures are calculated by the recursive Green's function method [18] implemented in NEMO5 [19] in an energy range between −2 and 2 eV around the Fermi level with a Brillouin zone sampled with a $30 \times 30 \times 1$ mesh. The integrated transmission spectra in the k space obtained by the tight-binding methods are compared against the spectrum obtained by the *ab initio* method with a similar basis set, energy cutoff, and Brillouin mesh, as is used in the ionic relaxation. The integrated transmission over the k space for the CSL plotted in Fig. 4 shows that the EH method captures the main features of DFT not only at the Fermi energy (E_f) but also over a large energy window. On other hand, while the transmission spectrum calculated by the TB method also shows reasonable agreement with DFT around the Fermi window, it fails to describe the *ab initio* transmission spectrum for energies away from the E_f. In order to validate our tight-binding models for more complex and disordered systems as described in Fig. 3, a transmission spectrum is calculated for the RS structures as shown in Fig. 5. Similar to the transmission spectrum obtained for the CSL (see Fig. 4), the EH model again captures the main features of DFT, while the TB model partially matches the results close to the Fermi energy, but it does not provide a good description of the electronic properties in a large energy window.

Subsequently, the resistance for the CSL and RS GBs in the ballistic limit is obtained based on the Landauer formalism assuming a low bias condition [20] as

$$G = \frac{1}{R} = \frac{2e^2}{h} \int T(E_f, \mathbf{k}) d^2k, \tag{1}$$

where G is the conductance, R is the resistance, e is the elementary charge, h is Planck's constant, and $T(E_f, \mathbf{k})$ is the transmission for a particular wave vector $\mathbf{k}$ at the Fermi energy. The Fermi levels in Figs. 1, 4, and 5 are calculated at the leads of the device self-consistently for DFT and non-self-consistently for tight-binding models. In this last case, the Fermi level is obtained by integrating over the DOS from $-\infty$ to E_f until this value becomes equal to the total number of electrons at a zero- temperature approximation [21]. Following Ref. [5], the specific resistances of the CSL and RS grain boundaries are obtained by $\gamma^R = (R - R_B)A$, where R is the resistance of the configuration that contains the GB, R_B is the resistance of the perfect bulk copper, and A is the grain cross section. The specific resistances for those CSL configurations are calculated by the TB and EH methods and compared to DFT as shown in Table I. The results in Table I and Fig. 6 show less than 10.4% difference in the specific resistance between the EH and DFT methods and less than 11.2% between the TB and DFT methods. Thus, the atomistic methods (TB and EH) are able to describe copper interconnects with reasonable accuracy.

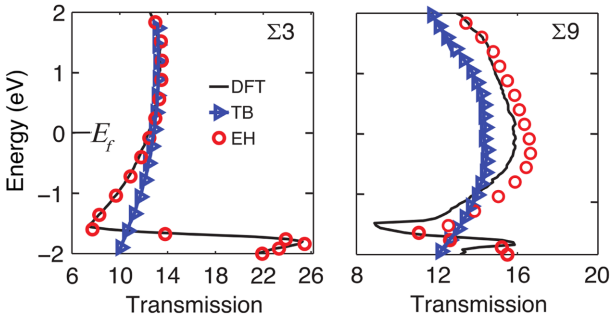

FIG. 4. Transmission spectra $T(E)$ for two different CSLs (Σ3 and Σ9) show that the EH model captures the main features of DFT.

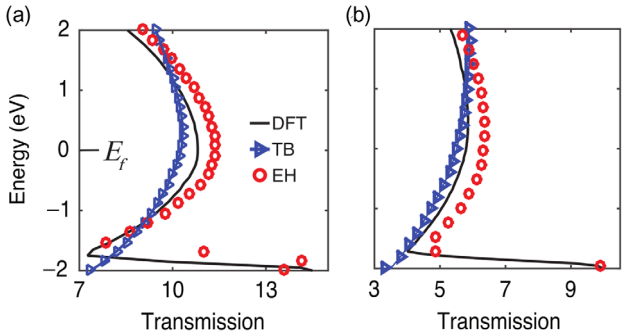

FIG. 5. Transmission spectra $T(E)$ for the RS structures (a) and (b) sketched in Fig. 3. The results show that tight-binding models describe the electronic properties for complex and disordered systems, but as before, the EH method captures the main features of DFT, while the TB method partially matches the results close to the Fermi energy

TABLE I. Specific resistance for different CSLs (ΣN) calculated by the TB, EH, and DFT methods.

GB	Specific resistance CSL γ^R (10^{-12} $\Omega\,cm^2$)				
	γ_{DFT}	γ_{EH}	γ_{TB}	Experiment	Other references
$\Sigma3$	0.156	0.173	0.158	0.170 [22]	0.202 [6] 0.155 [8] 0.158 [5] 0.148 [9]
$\Sigma5$	1.759	1.934	2.240		1.885 [6] 1.49 [5]
$\Sigma9$	1.82	1.72	2.14		1.75 [5]
$\Sigma11$	0.64	0.57	0.71		0.75 [5]
$\Sigma13$	2.01	1.72	2.09		2.41 [5]
Random 1	5.11	4.61	5.33		
Random 2	6.54	5.92	6.60		

These methods are chosen to study GB systems with 10^3 to 10^4 atoms because they require significantly fewer computer resources than the *ab initio* calculations [21].

Only *non-ab-initio* methods are capable of relaxing structures of this size ($\gg 10^3$ atoms); therefore, a force-field potential method based on an embedded atom model (EAM) is used. The relaxation is performed using LAMMPS software package [23] with an EAM potential constructed by Mishin *et al.* that is fitted to first-principles calculations to correctly describe grain boundaries and point defects in copper [24].

The accuracy of this approach is determined by comparing the formation energy for CSL GBs obtained by the *ab initio* and EAM methods. The formation energy γ^E is defined as follows:

$$\gamma^E = \frac{E_{slab} - NE_0}{A}, \tag{2}$$

where E_{slab} is the total energy of a slab configuration that contains a CSL GB, N is the number of atoms in the CSL GB, E_0 is the energy of a single atom of bulk copper, and A the cross-sectional area. The ionic relaxation carried out by *ab initio* methods uses the plane-wave DFT package (VASP) [25] and a PBE GGA exchange-correlation functional. The plane-wave energy cutoff is 500 eV and the Brillouin zone is sampled with a $4 \times 4 \times 1$ mesh until all atomic forces on each ion are less than 10^{-5} eV/Å. A comparison of the relaxation energy computed using the EAM potential with the DFT result (see Fig. 7) shows that the difference is less than 7% with for all CSL orientations except the Σ_{11}, which shows a larger error of 20%. These results indicate that the EAM potential calculation is an acceptable method to relax the grain-boundary structures with the benefit of reduced computational burden compared to DFT.

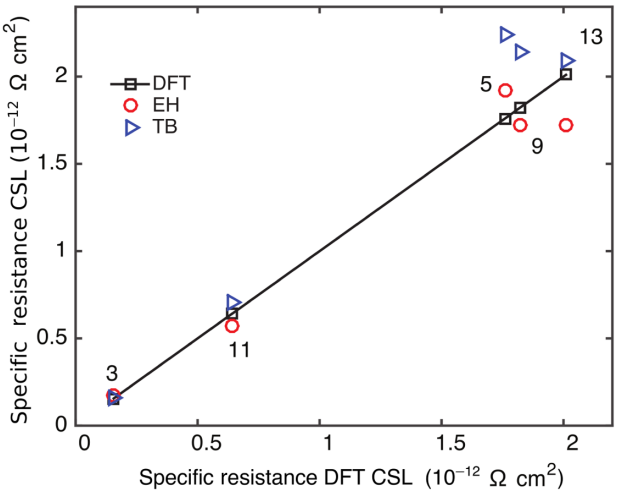

FIG. 6. Resistivities for different CSLs labeled by ΣN and calculated by the TB and EH methods and compared with the DFT method.

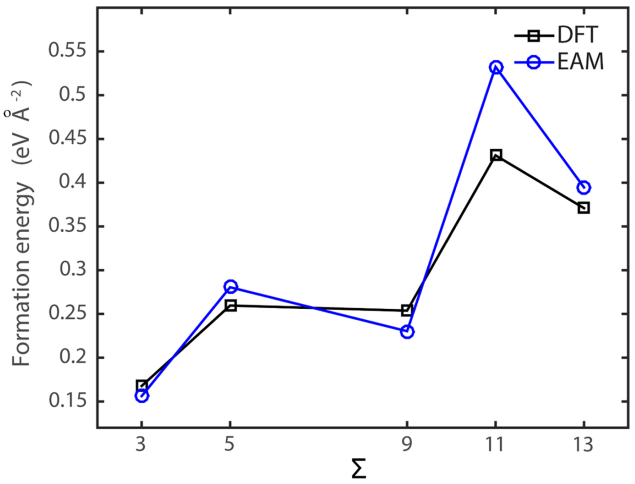

FIG. 7. Formation energy (γ^E) for different CSL GBs labeled by ΣN relaxed by the DFT and EAM potential.

IV. SPECIFIC RESISTANCE FOR GRAINS OF 10 nm LENGTH

Based on the prediction of the ITRS road map that interconnects will reach 10 to 30 nm length in the coming years [1], a set of copper thin films of 30 nm is constructed and modeled by the tight-binding methods as we describe in Sec. II. The copper interconnects are formed by three grains of 10 nm length. Each grain is constructed with a supercell growing in the [110] orientation with a lattice constant of 0.361 nm which has the highest conductance [10], as reported experimentally [14]. In order to quantify the effect of GB orientation on the specific resistances for copper interconnects, two different types of GBs are generated by Voronoi diagrams [17]. These GB types are based on the rotation direction of the middle grain shown as "tilt" and "twist" GBs, respectively, which generates two boundaries as shown in Figs. 8(a) and 8(b). Note that the rotations about the [110] axis are not studied in this work because it requires the simulation of a structure with a very large cross section due to the periodic conditions in the transverse direction which is beyond the authors' computational capabilities.

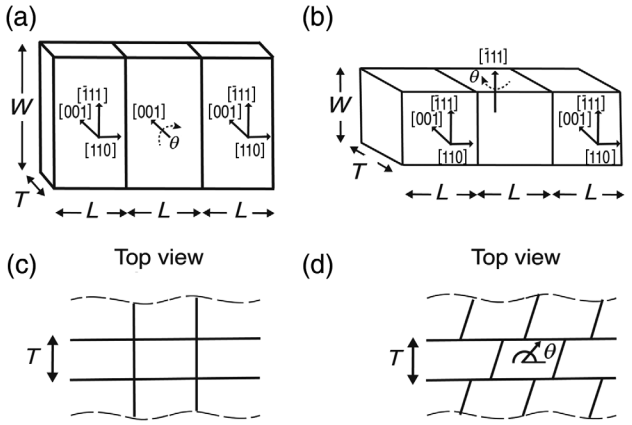

FIG. 8. GB classification: (a) Tilt GBs are generated by a rotation in the [001] plane. (b) Twist GBs generated by a rotation in the $[\bar{1}01]$ plane where the grain boundary is always perpendicular to the transport direction. (c) and (d) represent the top view of tilt and twist GB configurations.

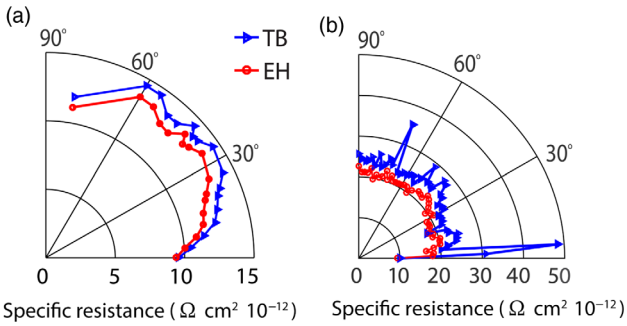

FIG. 9. (a) Tilt and (b) twist GB-specific resistance calculated by the TB and EH methods.

In order to have a lower impact on the specific resistance due to the electrode setup, three grains are modeled in this work. In both configurations, only the middle GB is initially rotated, then a periodic boundary condition is applied in the [001] direction for the ionic relaxation and the electronic transport calculation. Therefore, atomic surface roughness is present in the structures as a result of the relaxation. Additionally, it is assumed that each configuration shown in Figs. 8(a) and 8(b) is connected to a pristine source and drain lead oriented in the [110] direction, whose atoms are fixed during the ionic relaxation.

The tilt GBs are generated by a rotation of the middle grain with respect to the [001] direction by an angle θ in a range between 0° and 90°. Each grain is formed by a supercell of 10 nm length (L) in the transport direction [110], 10 nm width (W) in the $[\bar{1}01]$ direction, and 0.361 nm thickness (T) in the periodic direction [001], as shown in Figs. 8(a) and 8(c).

The twist GBs are generated by a rotation of the middle grain with respect to the $[\bar{1}11]$ direction by an angle θ in a range between 0° and 90°. The rotation is applied in the same direction as the periodicity; therefore, thicker grains are constructed to ensure the grains overlap after rotation. In this configuration setup, each grain is formed by a supercell of 10 nm length (L) in the transport direction [110], 3 nm width (W) in the $[\bar{1}01]$ direction, and 3 nm thickness (T) in the periodic direction [001] as shown in Figs. 8(b) and 8(d).

It is important to clarify that after any rotation for tilt or twist GB, the [110] direction is no longer the transport direction for that grain. Similarly, the rotation angle corresponds to the initial value, but this value will be slightly modified after relaxing the structure.

The specific resistance for tilt and twist GBs for different orientations is obtained by a procedure similar to that described in Sec. III as $\rho = R \times A$, where R is obtained by Eq. (1), and each configuration is relaxed by an EAM potential. Note that this value is different with respect to the specific resistance calculated for the CSL, because this time, it is not subtracted from the bulk contribution that corresponds to around 9.8 $\Omega\,\mathrm{cm}^2 \times 10^{-8}$ as shown in Fig. 9. In order to compare the specific resistance for tilt and twist GBs for different angles θ, the tilt GB values are normalized such that tilt and twist GBs are calculated over the same cross-sectional area. Those values are plotted in Fig. 9. In both systems, the specific resistance increases with an increase in the angle until the angle reaches 30°, and then it becomes almost constant, although the tilt GB shows a reduction after 60°. The specific resistance dependence for twist GBs shows more noise than for tilt GBs because the twist structure has more points per unit area where the grain boundaries intersect [see Figs. 8(c) and 8(d)], which leads to a higher number of dislocations.

To further understand the relationship between specific resistance and the orientation angle for the tilt grain boundaries (see Fig. 8), local density of states (LDOS) at the Fermi energy are calculated by the TB method as shown in Fig. 10. Five distinct regions can be observed in the LDOS for both configurations. The contacts (I and V), which are coupled to the central regions (II–IV), are not relaxed as previously described. As expected, the LDOS in these two areas is smooth and independent of the angle mismatch between the grains. In contrast, regions II, III, and IV show change with respect to the rotation angle. This result shows that the LDOS is perturbed not only at the grain boundary but rather over the entire grain. This contradicts the assumption of the Mayadas-Shatzkes model [4,26,27], which treats the grain-boundary effect as a local perturbation of the potential at the interface between grains. The LDOS of each grain is affected by the rotation of the middle grain, even though regions II and IV are not rotated.

As Fig. 9(a) shows, the configuration with rotation angle equal to 18° [which corresponds to Fig. 10(a)] has smaller specific resistance than the configuration with a 54° angle [Fig. 10(b)]. There is a comparatively lower LDOS in the

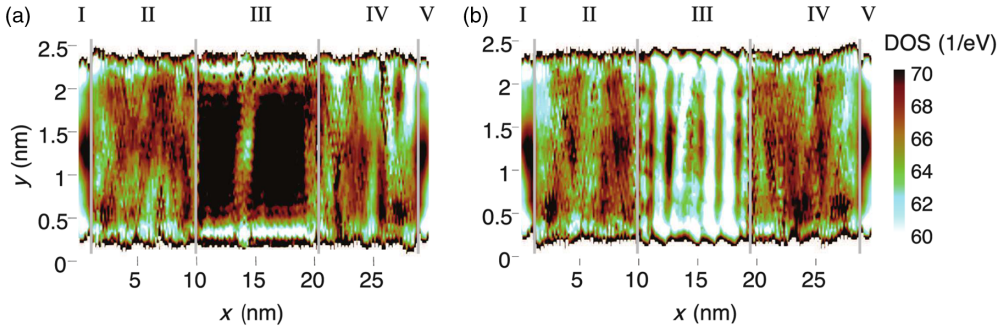

FIG. 10. LDOS calculated with the EH basis for tilt GBs rotated 18° (a) and 54° (b), respectively, about the [001] axis.

central region of Fig. 10(b); therefore, electrons will have fewer states to move into, increasing the specific resistance. Finally, the LDOS is higher at the surface where the atoms have dangling bonds.

As we describe in Sec. III, the simulations performed with the TB and EH methods exhibit the same specific resistance at the Fermi energy for the CSL and small random structures with an error of around 11% compared to first-principles calculations. However, the states beyond the Fermi level are not captured as well by the TB method. Therefore, in a much larger and more disordered structure, the TB model results are expected to differ from the EH results. However, surprisingly large values of specific resistance are observed for the twist GBs at 4° and 68° [Fig. 9(b)]. The authors suspect that the peaks in the specific resistance for the TB model in the twist configuration [Fig. 9(b)] are the result of an incomplete description of the coupling elements of the Hamiltonian corresponding to the coupling between copper atoms at the surface. In order to examine this issue, the number of atoms at the surface at a depth of 0.5 nm is calculated for each orientation as shown in Fig. 11(b). The results show that the two orientations that exhibit peaks in specific resistance (4° and 68°) show a large number of atoms at the surface (around 15% to 19% more with respect to the orientation at 2°). We also find that those configurations have a much larger mean distance to the first nearest neighbor as shown in Fig. 9(c). Those two orientations may contain a larger number of atoms that are beyond the cutoff distance used by the TB model (0.4 nm [10]), and the missing couplings may cause a nonphysical increase in the specific resistance. Note that the TB model is purposely parametrized for a cutoff of 0.4 nm [10]; in order to use a larger cutoff, the model must be reparametrized. However, this will make its numerical load nearly equivalent to the EH model, which does not have such a problem because it has a much larger interaction radius.

In order to create a compact model to predict how specific resistance changes as a result of GB orientation, a set of 600 samples is generated with geometries similar to the tilt configuration. The tilt configuration is chosen over the twist systems because the twist GBs require a much larger thickness beyond our computing power [see Figs. 8(b) and 8(d)].

Each GB is constructed with three grains, and each of them is rotated with an angle (α, β, γ) in a range between 0° and 180° parallel to the GB boundary. The dimensions of the GB are similar to those used for the tilt GB with thickness, width, and length equal to 0.5, 3, and 10 nm, respectively, as shown in Fig. 12. A periodic boundary condition in the [001] direction is imposed.

The specific resistance for these samples is calculated with the EH method because it is more reliable over angle rotations than the TB method. Making use of the results obtained from these samples, a box plot for α and γ in a range between 0° and 180° and a constant angle β is plotted

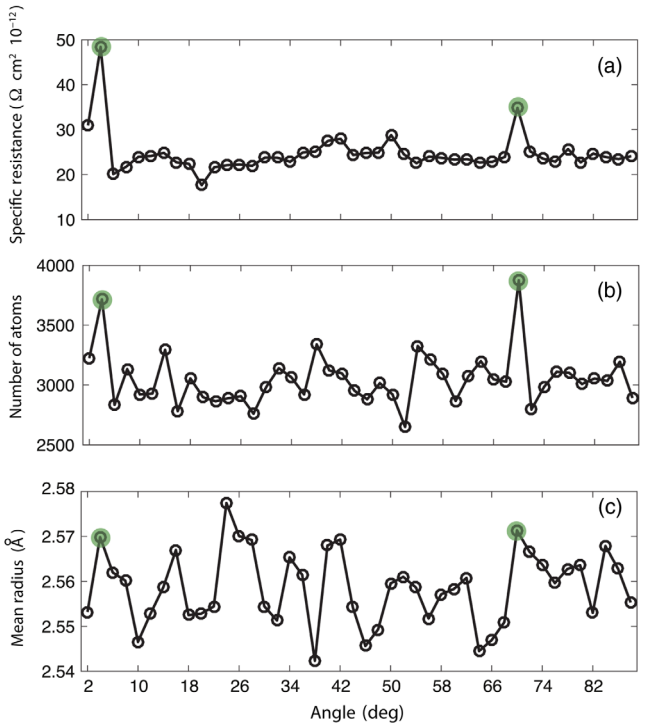

FIG. 11. (a) Resistivity, (b) mean radius, and (c) number of atoms for twist grain boundaries for different misorientation angles between 2° and 88° calculated with the TB model. The values 2° and 68° circled on the plots above correspond to the cases that present a large resistance. Those states exhibit a much larger mean first nearest-neighbor distance and number of atoms over the surface which are not correctly captured by our TB model that has a 2NN cutoff.

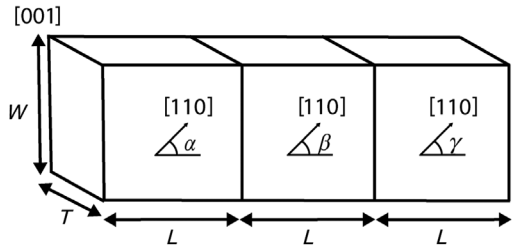

FIG. 12. GB configuration constructed with three grains, each one generated by rotating the lattice through angles α, β, γ, respectively, around the [001] axis.

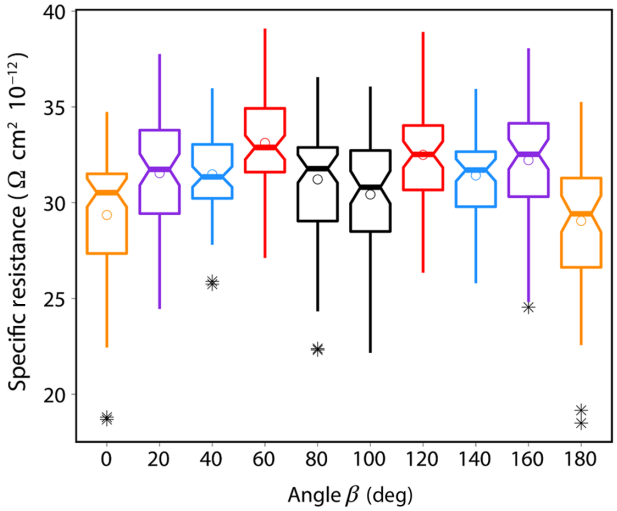

FIG. 13. Resistivity distributions for α and γ between 0∘ and 180∘ and a constant angle β. The box plots represent the resistance distribution, while those marked with a star represent outliers.

in Fig. 13, which shows a symmetry in the specific resistance in a range between 0° and 90° and 90° and 180°. This observation is confirmed by a statistic nonparametric Kolmogorov-Smirnov test [28], which compares the distribution function for the group of samples in a range between 0° and 90° against those between 90° and 180° and finds that both groups of samples are drawn from an equivalent continuous distribution. A p value of 0.16 is obtained for the Kolmogorov-Smirnov test, confirming that there is no difference between the specific resistance distributions for both cases with a confidence of 95%. The symmetry in the specific resistance is due to the fact that the crystal symmetry of copper is not totally disrupted by the structural relaxation. The probability distribution for the three different angles (α, β, and γ) in a range between 90° and 180° is plotted in Fig. 14.

Per the Shapiro-Wilk test [28] with a p value of 0.15% and 95% confidence, the specific resistance distribution follows a normal distribution with a mean and standard deviation equal to 31.7×10^{-12} and 2.8×10^{-12} $\Omega\,\mathrm{cm}^2$. The Q-Q plot in Fig. 14(b) shows that the specific resistance distribution is likely normal, although the left and right tails do not follow a normal distribution.

V. GRAIN BOUNDARIES MODELED BY A NEURAL NETWORK

Atomistic models based on a tight-binding approach can describe the effects of the GB orientation in the specific resistance for copper interconnects with the same accuracy as DFT methods but with a much lower computational burden. However, the specific resistance calculated by atomistic models such as the EH and TB models for a combination of three grains of 10 nm length in the transport direction are still not as fast as conventional models such as the Fuchs-Sondheimer and Mayadas-Shatzkes models [3,4], which describe surface roughness and grain-boundary effects, respectively, in copper interconnects. However, these models require experimental input to fit some parameters which limits the transferability for different configurations. Therefore, compact models based on the statistical results obtained from an atomistic model described in Sec. IV are proposed to describe the scattering effects on grain boundaries for a system of three grains of 10 nm length. Three different algorithms are used to construct the compact models, including a polynomial fit, a nearest-neighbor search model, and a neural network as described in the following subsections. The inputs for the compact models are the orientation angles α, β, and γ,

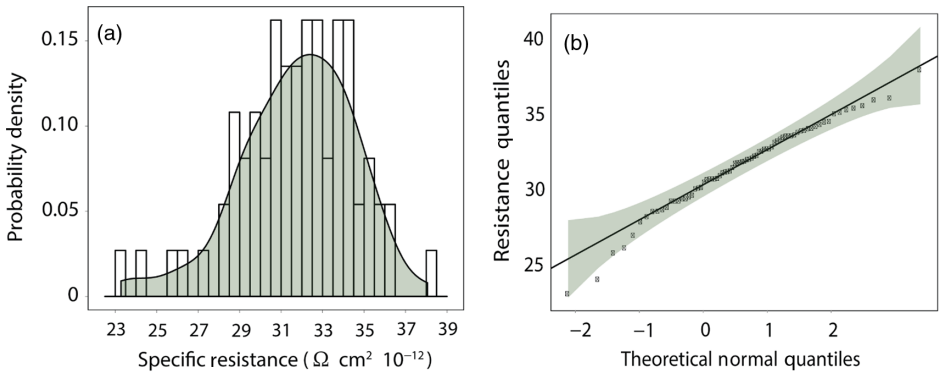

FIG. 14. (a) Probability distribution for a GB system rotated over three different angles α, β, and γ in a range between 90° and 180°. The shaded area represents the best approximation of a normal distribution for the 600 samples; (b) Q-Q plot which confirms the normal distribution.

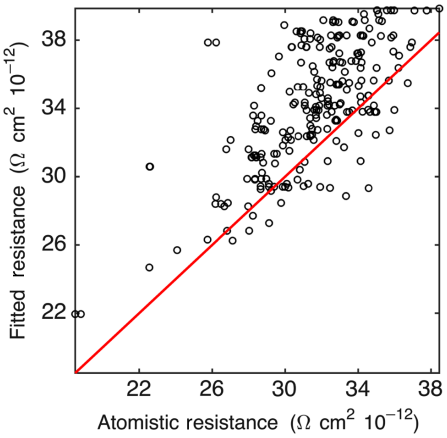

FIG. 15. Evaluation of the specific resistance for the multivariate polynomial model using a least-squares adjustment for the remaining 20% of the $\rho(\alpha,\beta,\gamma)$ values for copper interconnects.

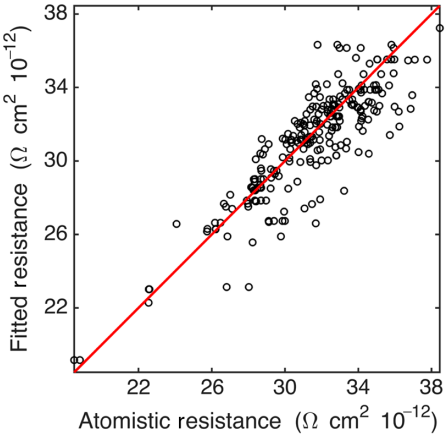

FIG. 16. Evaluation of the specific resistance for the nearest-neighbor model for the remaining 20% of the $\rho(\alpha,\beta,\gamma)$ values for copper interconnects.

and the output is the specific resistance of the GB $\rho(\alpha,\beta,\gamma)$. The compact models are trained with a random selection of 80% of the 600 samples plotted in the Fig. 14 and validated with the remaining 20% of the data.

A. Polynomial fit

A polynomial fit of second order is carried out based on a least-squares adjustment obtaining the following parametric relationship between the misorientation angles (α,β,γ) and the specific resistance:

$$\rho(\alpha,\beta,\gamma) = 21.95 + 10.59\alpha - 2.76\alpha^3 + 10.54\beta - 6.15\beta^2 + 13.41\gamma - 3.91\beta\gamma - 5.18\gamma^2. \quad (3)$$

The expected values obtained from the model are compared against the remaining 20% of the atomistic data as shown in Fig. 15. The parametric fitting based on a polynomial approximation with eight relevant parameters displays a poor match with the atomistic results with a 70% variability of the specific resistance for the training data set and a mean square error (MSE) equal to $13.94\times10^{-12}\,\Omega\mathrm{cm}^2$. This result shows that grain-boundary effects cannot be modeled as a simple additive effect between each orientation. Therefore, a more complicated dependence exists between the specific resistance and the orientation angles.

B. Nearest-neighbor fitting

Since the polynomial fit provides a poor fitting for the specific resistance of a GB oriented by the angles (α,β,γ), a nonparametric model is explored based on a "nearest-neighbor" search which uses the "dsearchn" triangulation method to determine the number of nearest neighbors for each query instance. Then, a linear interpolation between the nearest neighbors is carried out to obtain the interpolated value as implemented in the MATLAB optimization package [29]. The comparison between the expected and predicted specific resistance obtained with the process described before is plotted in Fig. 16. The mean square error obtained by this method is equal to $2.67\times10^{-12}\,\Omega\mathrm{cm}^2$, which is much lower than the error of the polynomial method. This method does not introduce any new parameters for interpolation, but it is limited by the dimensionality of the parametric space [30–32]; systems with a larger number of grains than are considered in this study will have a comparatively larger MSE.

C. Neural network model

Finally, a compact model based on a neural network [33] algorithm is introduced. Neural network models have been widely used to model complex problems; in the TB approach, neural network algorithms have been used to describe potential minimization [34] and material parametrization [35]. In this work, a multilayer neural network (MLN) is applied with a back-propagation algorithm [33] to quickly obtain the specific resistance of the GB. The neural network shown in Fig. 17 is achieved after testing different types of neural networks and varying the number of hidden layers. The final system is formed by an input layer, three hidden layers, and one output layer. The input layer $p=(\alpha,\beta,\gamma)$ is represented by a row vector of dimension 3×1. The hidden layer is composed of three inner layers i with 10, 6, and 3 neurons, respectively; the weight $\boldsymbol{W}^i$ and bias $\boldsymbol{b}^i$ vectors for a given layer i are shown in Fig. 17. The MLN is implemented in the statistical software R making use of the package NEURALNET[36]. The value of the parameters $\boldsymbol{W}^i$ and bias $\boldsymbol{b}^i$ are obtained by the gradient descent method [37], which minimizes the mean square error of the output layer. In the neural network, the functions $\boldsymbol{f}^i$ represent logistic functions employed at each

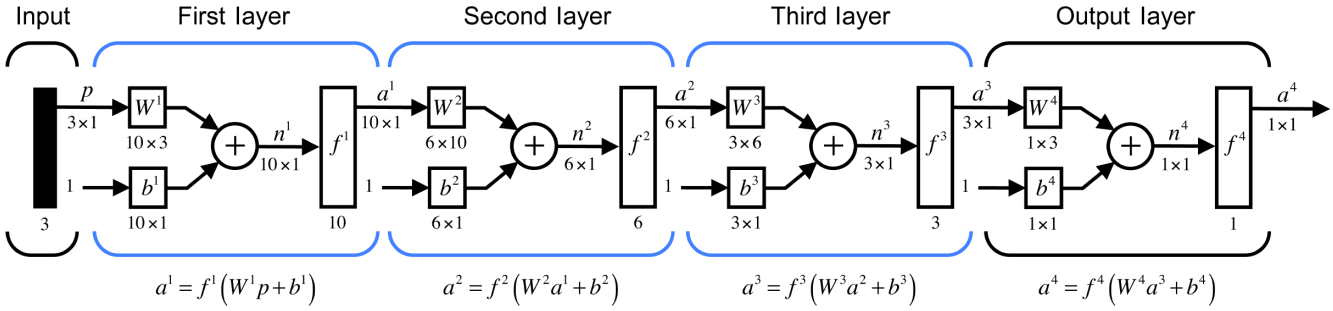

$$a^4 = f^4\left(W^4 f^3\left\{W^3 f^2\left[W^2 f^1\left(W^1 p + b^1\right) + b^2\right] + b^3\right\} + b^4\right)$$

FIG. 17. Schematic representation for the multilayer neural network used to describe grain-boundary-specific resistance for copper interconnects with three grains. The values $\boldsymbol{W}^i$ and $\boldsymbol{b}^i$ correspond to the weights and bias parameters, $\boldsymbol{f}^i$ represents logistic functions except for the last layer $\boldsymbol{f}^4$ to which is applied a linear function, and $a\boldsymbol{a}^i$ corresponds to the output at each neuron i.

layer, except for the last layer $\boldsymbol{f}^4$ to which is applied a linear function.

The MSE obtained by this model is equal to $1.44 \times 10^{-12}\ \Omega\,\mathrm{cm}^2$. The results obtained for the testing data of the MLN are plotted in Fig. 18; the model shows good agreement for low values of specific resistance and larger variability for GBs with a specific resistance over the range $(29.0\text{–}39.0) \times 10^{-12}\ \Omega\,\mathrm{cm}^2$. Though the neural network compact model requires many more parameters (131 parameters for this case) compared to the polynomial compact model and nearest-neighbor interpolation, it still has the lowest MSE while substantially reducing the computational burden in comparison to the full atomistic simulation. As observed in the literature, neural networks are recommended for the construction of nonparametric models [38–40] that can describe complex relations such as that between angle orientation and specific resistance. The neural network obtained in this work can exclusively model the specific resistance for systems with the geometric configurations described in Fig. 12 (the neural network is available from a Jupiter notebook [41]). However, the neural network sketched in Fig. 17 may be used as an initial guess for more complicated configurations with different geometries and number of grains, which cannot be described by nonparametric methods such as nearest neighbor or linear fitting.

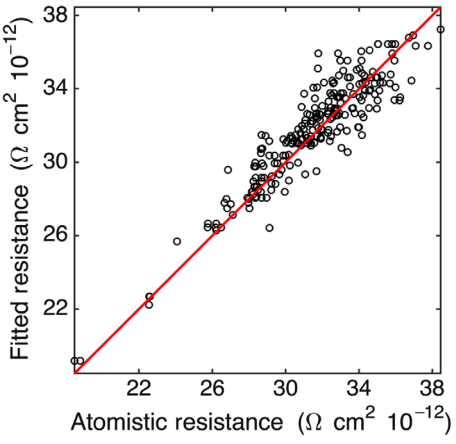

FIG. 18. Evaluation of the specific resistance for the multilayer neural network model for the remaining 20% of the $\rho(\alpha, \beta, \gamma)$ values for copper interconnects.

VI. SUMMARY

In summary, the effect of orientation on grain-boundary resistance for copper interconnects is studied using two different atomistic tight-binding methods (EH and TB). The transmission spectrum and specific resistance calculated by these methods are benchmarked for a coincident site lattice single GB (ΣN) against first-principles calculations. These results show that the EH method captures the main features of DFT in the Fermi window between -2 and 2 eV. On other hand, the transmission spectrum calculated by the TB method also shows reasonable agreement with DFT around the Fermi window, but it fails to describe the *ab initio* transmission spectrum for energies away from the Fermi energy. Since the computational requirements for tight-binding methods are also much smaller than for first-principle calculations, the EH method is an effective way to describe the specific resistance of interconnects with lengths greater than 30 nm.

The LDOS obtained with the atomistic model shows that the perturbation in the LDOS is not at the grain boundary but rather over the entire grain. This contradicts the assumption of the Mayadas-Shatzkes model [4,26,27], which models the grain-boundary effect as a local perturbation of the potential at the interface between grains.

Orientation effects for tilt and twist GBs for copper interconnects of 30 nm length relaxed by a semiclassical

EAM potential are also benchmarked against first-principles calculations. Rotations perpendicular to the transport direction have a larger effect on the specific resistance of the GB than rotations parallel to the transport direction. Statistical analysis of GB-specific resistance shows that the inversion symmetry of copper is still manifested for the considered grain geometry.

Finally, statistical models based on three different algorithms are studied. The parametric model based on a polynomial fit of the misorientation angles (α, β, γ) shows a poor match with the test results from the atomistic model, confirming that a complex relationship exists between the specific resistance and orientation angles. While the nearest-neighbor model displays a better fit with an error of $2.67 \times 10^{-12}\ \Omega\,\mathrm{cm}^2$, it can support only 3 degrees of freedom. Among the studied models, the compact model based on a neural network is the best algorithm to describe the specific resistance with a MSE lower than $1.44 \times 10^{-12}\ \Omega\,\mathrm{cm}^2$. As mentioned before, the neural network obtained in this work is validated only for the systems analyzed in Fig. 12. However, the neural network sketched in Fig. 17 may be used as an initial guess for a system with more degrees of freedom, as well as for configurations with different geometries or number of grains.

In this manuscript, the ballistic resistance due to the grain-boundary effect is studied. While electron-phonon scattering is reported to play an important role in copper resistivity at room temperature and when the grains are larger [2,42], these effects are not included in this work. Future work will use the neural network to generate a compact model that includes electron-phonon scattering in addition to grain-boundary effects to describe the resistivity for copper interconnects.

ACKNOWLEDGMENTS

This work is supported by the FAME Center, one of six centres of STARnet, a Semiconductor Research Corporation program sponsored by MARCO and DARPA. Support by the U.S. Department of Energy National Nuclear Security Administration under Grant No. DE-FC52-08NA28617 is acknowledged. The authors also acknowledge the staff and computing resources of both the Rosen Center for Advanced Computing at Purdue University and the Blue Waters sustained-petascale computing project, which is supported by the National Science Foundation (Grant No. ACI 1238993). Finally, the authors would like to thank Dr. Bozidar Novakovic and David Guzman for stimulating discussions about the topic.

APPENDIX: ENVIRONMENTAL TIGHT BINDING PARAMETERS

Parameters for bulk copper with the environmental TB method are obtained by direct fitting bulk band structure [10], but additional constraints on the interatomic coupling are included during the parametrization process.

TABLE II. TB parameters for Cu following the notation of Ref. [10].

Parameter name	Value	Parameter name	Value
VBO	3.6540	$I\_D\_D\_\Delta$	−0.08
E_S	−4.5236	$q\_D\_D\_\sigma$	4.8355
E_Px	−0.1458	$q\_D\_D\_\Pi$	4.7528
E_Py	−0.1458	$q\_D\_D\_\Delta$	4.2950
E_Pz	−0.1458	$I\_S\_S\_\sigma$	0.4
E_Dxy	−4.3034	$I\_S\_P\_\sigma$	0.4457
E_Dyz	−4.3034	$I\_S\_D\_\sigma$	−0.36819
E_Dxz	−4.3034	$I\_P\_P\_\sigma$	1.5605
E_Dz^2	−4.3034	$I\_P\_D\_\sigma$	−0.2532
$E\_Dx^2\_y^2$	−4.3034	$I\_P\_P\_\Pi$	−0.1348
$V\_S\_S\_\sigma$	−0.9588	$I\_P\_D\_\Pi$	0.0135
$V\_S\_P\_\sigma$	1.4063	$q\_S\_S\_\sigma$	2.20333
$V\_S\_D\_\sigma$	−0.1841	$q\_S\_P\_\sigma$	2.6554
$V\_P\_P\_\sigma$	1.4025	$q\_S\_D\_\sigma$	0.2495
$V\_P\_P\_\Pi$	−0.5730	$q\_P\_P\_\sigma$	1.5905
$V\_P\_D\_\sigma$	−0.4607	$q\_P\_P\_\Pi$	2.9059
$V\_P\_D\_\Pi$	0.3373	$q\_P\_D\_\sigma$	3.8124
$V\_D\_D\_\sigma$	−0.3709	$q\_P\_D\_\Pi$	3.9330
$V\_D\_D\_\Pi$	0.2760	$p\_S\_S\_\sigma$	1.3692
$V\_D\_D\_\Delta$	−0.0735	$p\_S\_P\_\sigma$	2.8794
$I\_D\_D\_\sigma$	−0.15	$p\_S\_D\_\sigma$	3.94296
$I\_D\_D\_\Pi$	−0.2498	$p\_P\_P\_\sigma$	5.5023
$p\_P\_P\_\Pi$	0.536231	$p\_P\_D\_\sigma$	−1.0
$p\_P\_D\_\Pi$	−1.0	$p\_D\_D\_\sigma$	−0.83723
$p\_D\_D\_\Pi$	0.66507	$p\_D\_D\_\Delta$	4.8475
R_0_inter	0.25526	R_0_intra	0.25526

[1] International roadmap for semiconductors, http://public.itrs.net/reports.html.

[2] R. L. Graham, G. B. Alers, T. Mountsier, N. Shamma, S. Dhuey, S. Cabrini, R. H. Geiss, D. T. Read, and S. Peddeti, Resistivity dominated by surface scattering in sub-50 nm Cu wires, Appl. Phys. Lett. **96**, 042116 (2010).

[3] K. Fuchs and N. F. Mott, The conductivity of thin metallic films according to the electron theory of metals, Math. Proc. Cambridge Philos. Soc. **34**, 100 (1938).

[4] A. F. Mayadas, Electrical resistivity model for polycrystalline films: The case of specular reflection at external surfaces, Appl. Phys. Lett. **14**, 345 (1969).

[5] Mathieu César, Dongping Liu, Daniel Gall, and Hong Guo, Calculated Resistances of Single Grain Boundaries in Copper, Phys. Rev. Applied **2**, 044007 (2014).

[6] Tae-Hwan Kim, X.-G. Zhang, Don M. Nicholson, Boyd M. Evans, Nagraj S. Kulkarni, B. Radhakrishnan, Edward A. Kenik, and An-Ping Li, Large discrete resistance jump at grain boundary in copper nanowire, Nano Lett. **10**, 3096 (2010).

[7] Baruch Feldman, Seongjun Park, Michael Haverty, Sadasivan Shankar, and Scott T. Dunham, Simulation of grain boundary effects on electronic transport in metals, and

detailed causes of scattering, Phys. Status Solidi (b) **247**, 1791 (2010).
[8] Ben Zhou, Y. Xu, S. Wang, Guanghui Zhou, and K. Xia, An *ab initio* investigation on boundary resistance for metallic grains, Solid State Commun. **150**, 1422 (2010).
[9] X.-G. Zhang, Kalman Varga, and Sokrates T. Pantelides, Generalized Bloch theorem for complex periodic potentials: A powerful application to quantum transport calculations, Phys. Rev. B **76**, 035108 (2007).
[10] Ganesh Hegde, Michael Povolotskyi, Tillmann Kubis, Timothy Boykin, and Gerhard Klimeck, An environment-dependent semi-empirical tight binding model suitable for electron transport in bulk metals, metal alloys, metallic interfaces, and metallic nanostructures. I. Model and validation, J. Appl. Phys. **115**, 123703 (2014).
[11] Roald Hoffmann, A chemical and theoretical way to look at bonding on surfaces, Rev. Mod. Phys. **60**, 601 (1988).
[12] J. Cerdá and F. Soria, Accurate and transferable extended Hückel-type tight-binding parameters, Phys. Rev. B **61**, 7965 (2000).
[13] Mads Brandbyge, José-Luis Mozos, Pablo Ordejón, Jeremy Taylor, and Kurt Stokbro, Density-functional method for nonequilibrium electron transport, Phys. Rev. B **65**, 165401 (2002).
[14] M. E. Straumanis and L. S. Yu, Lattice parameters, densities, expansion coefficients and perfection of structure of Cu and of Cu-In α phase, Acta Crystallogr. Sect. A **A25**, 676 (1969).
[15] P. D. Bristowe and A. G. Crocker, The structure of high-angle (001) CSL twist boundaries in f.c.c. metals, Philos. Mag. A **38**, 487 (1978).
[16] Gbstudio, https://staff.aist.go.jph.ogawa/GBstudio/indexE.html.
[17] Chris H. Rycroft, Gary S. Grest, James W. Landry, and Martin Z. Bazant, Analysis of granular flow in a pebble-bed nuclear reactor, Phys. Rev. E **74**, 021306 (2006).
[18] Roger Lake, Gerhard Klimeck, R. Chris Bowen, and Dejan Jovanovic, Single and multiband modeling of quantum electron transport through layered semiconductor devices, J. Appl. Phys. **81**, 7845 (1997).
[19] Sebastian Steiger, Michael Povolotskyi, Hong-Hyun Park, Tillmann Kubis, and Gerhard Klimeck, NEMO5: A parallel multiscale nanoelectronics modeling tool, IEEE Trans. Nanotechnol. **10**, 1464 (2011).
[20] Supriyo Datta, *Electronic Transport in Mesoscopic Systems* (Cambridge University Press, Cambridge, England, 1997).
[21] Daniel Valencia, Evan Wilson, Prasad Sarangapani, Gustavo A. Valencia-Zapata, Gerhard Klimeck, Michael Povolotskyi, and Zhengping Jiang, in *Proceedings of the 2016 International Conference on Simulation of Semiconductor Processes and Devices (SISPAD)* (IEEE, New York, 2016), pp. 105–108.
[22] Lei Lu, Yongfeng Shen, Xianhua Chen, Lihua Qian, and K. Lu, Ultrahigh strength and high electrical conductivity in copper, Science **304**, 422 (2004).
[23] Steve Plimpton, Fast parallel algorithms for short-range molecular dynamics, J. Comput. Phys. **117**, 1 (1995).
[24] Y. Mishin, M. J. Mehl, D. A. Papaconstantopoulos, A. F. Voter, and J. D. Kress, Structural stability and lattice defects in copper: *Ab initio*, tight-binding, and embedded-atom calculations, Phys. Rev. B **63**, 224106 (2001).
[25] G. Kresse and J. Furthmüller, Efficiency of *ab-initio* total energy calculations for metals and semiconductors using a plane-wave basis set, Comput. Mater. Sci. **6**, 15 (1996).
[26] A. F. Mayadas and M. Shatzkes, Electrical-resistivity model for polycrystalline films: The case of arbitrary reflection at external surfaces, Phys. Rev. B **1**, 1382 (1970).
[27] D. Josell, A paradigm for interconnect geometry to reduce grain boundary resistance, J. Appl. Phys. **100**, 123705 (2006).
[28] W. J. Conover, *Practical Nonparametric Statistics*, 3rd ed. (Wiley Publications, New York, 1999).
[29] MATLAB, Optimization Toolbox R2015a, MathWorks, 2015.
[30] Charu C. Aggarwal, Alexander Hinneburg, and Daniel A. Keim, in *Proceedings of the 8th International Conference on Database Theory, ICDT '01* (Springer-Verlag, London, 2001), pp. 420–434.
[31] Arthur Flexer and Dominik Schnitzer, Choosing p norms in high-dimensional spaces based on hub analysis, Neurocomputing **169**, 281 (2015).
[32] Dominik Schnitzer, Arthur Flexer, Markus Schedl, and Gerhard Widmer, Local and global scaling reduce hubs in space, J. Mach. Learn. Res. **13**, 2871 (2012).
[33] M. Hagan, H. Demuth, and M. Beale, *Neural Network Design* (PWS Publishing Company, Boston, MA, 1996), p. 734.
[34] L. R. Marim, M. R. Lemes, and A. Dal Pino, Neural-network-assisted genetic algorithm applied to silicon clusters, Phys. Rev. A **67**, 033203 (2003).
[35] A. Bholoa, S. D. Kenny, and R. Smith, A new approach to potential fitting using neural networks, Nucl. Instrum. Methods Phys. Res., Sect. B **255**, 1 (2007).
[36] F. Guenther and S. Fritsch, *NEURALNET: Training of Neural Networks* (The R Foundation, Vienna, 2010), Vol. 2, p. 30.
[37] S. Haykin, *Neural Networks—A Comprehensive Foundation*, 2nd ed. (Prentice-Hall, Englewood Cliffs, NJ, 1999).
[38] Christopher M. Bishop, *Pattern Recognition and Machine Learning*, 1st ed., Information Science and Statistics (Springer-Verlag, New York, 2006).
[39] Claude Sammut and Geoffrey I. Webb, *Encyclopedia of Machine Learning*, 1st ed. (Springer Publishing Company, Incorporated, New York, 2011).
[40] S. J. Raudys and A. K. Jain, Small sample size effects in statistical pattern recognition: Recommendations for practitioners, IEEE Trans. Pattern Anal. Mach. Intell. **13**, 252 (1991).
[41] Daniel Valencia, Gustavo A. Valencia-Zapata, Daniel F Mejia, Kuang-Chung Wang, Gerhard Klimeck, and Michael Povolotskyi, Specific resistance for copper interconnects, https://nanohub.org/resources/27576, 2017.
[42] J. J. Plombon, Ebrahim Andideh, Valery M. Dubin, and Jose Maiz, Influence of phonon, geometry, impurity, and grain size on copper line resistivity, Appl. Phys. Lett. **89**, 113124 (2006).